Ninth International Conference on Computational Fluid Dynamics (ICCFD9), Istanbul, Turkey, July 11-15, 2016

ICCFD9-2016-160

Aerodynamic Optimisation of Active Flow Control on a Three-Element High-Lift Configuration

Anil Nemili[1], Emre Özkaya[2], Nicolas R. Gauger[2], Felix Kramer[3], Frank Thiele[3]

[1] Department of Mathematics, BITS Pilani, Hyderabad Campus, Hyderabad 500078, India
[2] Chair for Scientific Computing, TU Kaiserslautern, 67663 Kaiserslautern, Germany
[3] CFD Software Entwicklungs- und Forschungsgesellschaft mbH, 14163 Berlin, Germany

Corresponding author: nicolas.gauger@scicomp.uni-kl.de

Abstract: This paper presents the optimal active flow control mechanism on the industry-relevant Swept Constant-Chord Half model (SCCH) high-lift configuration. To delay the separation, synthetic jet actuation is applied almost on the entire flap surface. Effective separation control and thus enhancement in overall aerodynamic performance can be achieved by finding the optimal actuation. In the present work, the optimal set of actuation parameters is obtained by combining the unsteady discrete adjoint incompressible RANS solver with the BFGS optimisation algorithm. Numerical results have shown that the optimal actuation has effectively delayed the onset of flow separation. Furthermore, optimal actuation has significantly enhanced the mean-lift coefficient by 28% over the un-actuated baseline flow.

Keywords: Active Flow Control, Synthetic Jets, High-Lift Configuration, Unsteady RANS, Discrete Adjoints, Algorithmic Differentiation

1 Introduction

Modern commercial aircraft deploy high-lift devices such as slats and flaps to generate additional amount of lift in order to reduce the ground speed and runway length during take-off and landing phases. At high flap deflection angles, the adverse pressure gradient becomes so strong that the boundary layer in the flap region tends to separate, leading to aerodynamic stall. This results in rapid degradation of aerodynamic performance as the lift falls abruptly. Over the past several decades, numerous flow control techniques have been proposed and evaluated for suppressing or even delaying the separation [1, 2, 3]. These approaches can be classified as passive or active flow control techniques. Compared to passive techniques, active control techniques are more desirable and widely used for the control of separation on generic high-lift devices [4, 5, 6, 7, 8, 9]. Although many subclasses exist, in recent years, active control techniques based on the zero-net-mass-flux or the synthetic jets have shown good feasibility and effectiveness in controlling separation.

Synthetic jet actuators [10, 11] are based on alternate injection and suction of fluid to the boundary layer with the formation of vortex structures. These vortices greatly enhance the boundary layer mixing. This increases the momentum transport inside and outside the boundary layer, which suppresses or delays the separation. The flow control is then achieved by varying the parameters of actuation such as amplitude, frequency, blowing directions, phase shift and location of actuators.

In previous studies on high-lift configurations, actuation is typically applied at the leading edge of the flap, where the flow starts separating from the surface. In the present work, we plan to apply actuation

almost on the entire flap surface. This distribution is intentionally chosen to avoid any bias on the location of actuators. Effective separation control and thus maximum lift can be achieved by finding the optimal distribution of actuation parameters. An efficient way of finding the optimal actuation parameters, which are in large number, is by employing the gradient based optimisation algorithms combined with discrete adjoint method. In [12], this approach is pursued to find the optimal actuation on the two-dimensional high-lift configuration. It has been observed that the adjoint based optimisation has significantly enhanced the mean-lift by 27% over the un-actuated baseline flow. In this paper, an attempt has been made to find the optimal actuation on the Swept Constant Chord Half (SCCH) model, which represents a generic high-lift configuration with industrial relevance. This test case has been extensively used to perform several experimental and numerical investigations of active flow control [13, 6, 14, 15, 8].

This paper is organised as follows. Section 2 presents the details pertaining to the development of an accurate and robust discrete adjoint approach for optimal active flow control, governed by unsteady incompressible RANS equations. In Section 3, we introduce the SCCH high-lift configuration, synthetic jet actuation boundary condition and features of the unsteady primal and adjoint RANS solvers. In Section 4, numerical results are shown based on optimal actuation. Finally, conclusions are drawn in Section 5.

2 A Discrete Adjoint Approach for Optimal Active Flow Control

We consider the optimisation problem of maximising the lift of the SCCH high-lift configuration by means of synthetic jet actuation. The objective function is defined as the time-averaged (mean) lift coefficient. The constraints are the incompressible unsteady Reynolds-averaged Navier-Stokes (RANS) equations, which govern the low speed flows during take-off and landing scenarios. The control variables are the amplitudes, phase shifts and blowing directions of actuation that are distributed on the suction side of the flap. In the discrete form, the objective function $\left(J = \overline{C}_l\right)$ over the time interval $[0, T]$ can be defined as

$$J = \overline{C}_l = \frac{1}{N} \sum_{n=1}^{N} I^n \left(\boldsymbol{U}^n, \boldsymbol{\alpha}\right), \; I^n = C_l^n \tag{1}$$

Here I^n is the lift coefficient at time iteration n. $\boldsymbol{U}^n$ is the state vector consisting of the velocity vector, pressure and turbulent quantities that describe the fluid motion. $\boldsymbol{\alpha}$ is the vector of control variables comprising the actuation parameters amplitude, frequency, phase shift and blowing angles. $N = T/\Delta t$ is the number of time iterations that span the given time interval and Δt is the step size of the time discretisation scheme. The governing unsteady incompressible RANS equations are discretised using the Finite Volume Method (FVM) on collocated grids. The spatial discretisation scheme is based on the SIMPLE pressure-velocity coupling scheme coupled with the Rhie-Chow interpolation. The transient terms are approximated by a second-order implicit backward difference formula.

At each time iteration n, the discretised constraint equations are solved for the solution of the state vector $\boldsymbol{U}^n$ by a contractive fixed point iterative scheme of the form

$$\boldsymbol{U}_{i+1}^n = G^n \left(\boldsymbol{U}_i^n, \boldsymbol{U}^{n-1}, \boldsymbol{U}^{n-2}, \boldsymbol{\alpha}\right), \; n = 1, \ldots, N. \tag{2}$$

Here, G^n represents an iteration of the pressure-velocity coupling scheme. $\boldsymbol{U}^{n-1}$ and $\boldsymbol{U}^{n-2}$ are the converged state vectors at time iterations $n-1$ and $n-2$ respectively. The fixed point scheme in Eq. (2) converges to the numerical solution $\boldsymbol{U}^n$, given by

$$\boldsymbol{U}^n = G^n \left(\boldsymbol{U}^n, \boldsymbol{U}^{n-1}, \boldsymbol{U}^{n-2}, \boldsymbol{\alpha}\right), \; n = 1, \ldots, N. \tag{3}$$

The Lagrangian associated with the constrained optimisation problem posed by Eqs. (1) and (3) is defined as

$$L = \frac{1}{N} \sum_{n=1}^{N} I^n \left(\boldsymbol{U}^n, \boldsymbol{\alpha}\right) - \sum_{n=1}^{N} \left\{ \left(\overline{\boldsymbol{U}}^n\right)^T \left[\boldsymbol{U}^n - G^n \left(\boldsymbol{U}^n, \boldsymbol{U}^{n-1}, \boldsymbol{U}^{n-2}, \boldsymbol{\alpha}\right)\right] \right\} \tag{4}$$

where $\overline{\boldsymbol{U}}^n$ is the vector of Lagrangian multipliers or the adjoint state vector at time iteration n. The first order necessary conditions for optimality (KKT) of the Lagrangian function are given by

$$\frac{\partial L}{\partial \overline{\boldsymbol{U}}^n} = 0, \quad n = 1, \ldots, N. \qquad \text{(State equations)} \tag{5a}$$

$$\frac{\partial L}{\partial \boldsymbol{U}^n} = 0, \quad n = N, \ldots, 1. \qquad \text{(Adjoint state equations)} \tag{5b}$$

$$\frac{\partial L}{\partial \boldsymbol{\alpha}} = 0 \qquad \text{(Control equations)} \tag{5c}$$

The above equations form an optimality system, from which optimal state and control vectors can be deduced. From Eq. (5b), the unsteady discrete adjoint RANS equations can be derived as

$$\begin{aligned}
\overline{\boldsymbol{U}}^n_{i+1} &= \left(\frac{\partial G^n}{\partial \boldsymbol{U}^n}\right)^T \overline{\boldsymbol{U}}^n_i + \frac{1}{N}\left(\frac{\partial I^n}{\partial \boldsymbol{U}^n}\right)^T, \quad n = N \\
\overline{\boldsymbol{U}}^n_{i+1} &= \left(\frac{\partial G^n}{\partial \boldsymbol{U}^n}\right)^T \overline{\boldsymbol{U}}^n_i + \left(\frac{\partial G^{n+1}}{\partial \boldsymbol{U}^n}\right)^T \overline{\boldsymbol{U}}^{n+1} + \frac{1}{N}\left(\frac{\partial I^n}{\partial \boldsymbol{U}^n}\right)^T, \quad n = N-1 \\
\overline{\boldsymbol{U}}^n_{i+1} &= \left(\frac{\partial G^n}{\partial \boldsymbol{U}^n}\right)^T \overline{\boldsymbol{U}}^n_i + \left(\frac{\partial G^{n+1}}{\partial \boldsymbol{U}^n}\right)^T \overline{\boldsymbol{U}}^{n+1} + \left(\frac{\partial G^{n+2}}{\partial \boldsymbol{U}^n}\right)^T \overline{\boldsymbol{U}}^{n+2} \\
&\quad + \frac{1}{N}\left(\frac{\partial I^n}{\partial \boldsymbol{U}^n}\right)^T, \quad n = N-2, \ldots, 1
\end{aligned} \tag{6}$$

Simplifying further, the adjoint pressure-velocity coupling scheme in the fixed point form is given by

$$\overline{\boldsymbol{U}}^n_{i+1} = \overline{G}^n\left(\boldsymbol{U}^n, \boldsymbol{U}^{n+1}, \boldsymbol{U}^{n+2}, \overline{\boldsymbol{U}}^n_i, \overline{\boldsymbol{U}}^{n+1}, \overline{\boldsymbol{U}}^{n+2}, \boldsymbol{\alpha}\right), \; n = N, \ldots, 1. \tag{7}$$

Here, $\overline{G}^n$ represents an iteration of the adjoint fixed point scheme, which converges to the adjoint solution $\overline{\boldsymbol{U}}^n$ at time iteration n. $\overline{\boldsymbol{U}}^{n+1}$ and $\overline{\boldsymbol{U}}^{n+2}$ are the converged adjoint solutions at time steps $n+1$ and $n+2$ respectively. In contrast to the primal fixed point scheme in Eq. (2), the adjoint scheme in Eq. (7) is solved in backward-in-time integration from $n = N$ to $n = 1$. The adjoint equations at time iteration n require the flow solutions $\boldsymbol{U}^n$, $\boldsymbol{U}^{n+1}$ and $\boldsymbol{U}^{n+2}$ to compute G^n, G^{n+1}, G^{n+2} and I^n. Thus, to solve the adjoint equations, one needs to store the entire forward trajectory of the non-linear primal solver. Note that $\frac{\partial G^{n+1}}{\partial \boldsymbol{U}^n}$ and $\frac{\partial G^{n+2}}{\partial \boldsymbol{U}^n}$ in Eq. (6) are constants as the spatial residuals in G^{n+1} and G^{n+2} do not depend on $\boldsymbol{U}^n$.

The solutions of the state and adjoint state equations are then substituted in Eq. (5c) to compute the sensitivity gradients as

$$\frac{dL}{d\boldsymbol{\alpha}} = \sum_{n=1}^{N}\left\{\frac{1}{N}\frac{\partial I^n}{\partial \boldsymbol{\alpha}} + \left(\overline{\boldsymbol{U}}^n\right)^T \frac{\partial G^n}{\partial \boldsymbol{\alpha}}\right\} \tag{8}$$

Accurate computation of the sensitivity gradients requires the exact differentiation of I^n and $\boldsymbol{G}^n$. However, the exact differentiation of the discrete residuals in $\boldsymbol{G}^n$ by hand is laborious and prone to errors. On the other hand, Algorithmic Differentiation (AD) [16] tools can perform the exact differentiation with much ease. In the present work, at the first step, AD is applied in a black-box fashion to generate the adjoint code by differentiating the unsteady incompressible RANS code with respect to the actuation control vector $\boldsymbol{\alpha}$. An advantage of the black-box AD approach is that the adjoint solver yields exact sensitivities at any residual level achieved by the primal solver. Furthermore, the adjoint solver inherits the asymptotic convergence of the primal solver [16].

A major drawback of the black-box approach is that the adjoint code demands prohibitively expensive memory and computational time, thus making it infeasible for practical applications. One source of excessive memory and run-time is due to the black-box application of AD to the fixed point scheme in Eq. (2), meant for the solution of the state vector at time iteration n. In this approach, the adjoint code stores the

flow solution $\boldsymbol{U}_{i+1}^{n}$ for all i iterations at every time step n. However, from Eq. (7) it can be observed that the adjoint fixed point scheme uses only the converged flow solution $\boldsymbol{U}^{n}$. Therefore, a lot of memory and run-time can be saved if we make use of the iterative structure and store only the converged flow solution at each unsteady time iteration. In the present work, this objective is achieved by employing the reverse accumulation technique [17].

Yet another source of expensive memory arises from the storage of flow solutions during the forward-in-time integration of the state equations in Eq. (2), which are then used while solving the adjoint equations in backward-in-time in Eq. (7). For large scale applications in $3D$, the memory requirements for storing the flow solutions can become prohibitively expensive. To reduce these excessive memory demands, checkpointing strategies can be employed. In algorithms based on checkpointing strategy, the flow solutions are stored only at selective time steps known as checkpoints. These checkpoints are then used to recompute the intermediate states that have not been stored. In the present work, the binomial checkpointing algorithm [18] has been employed. This algorithm generates the checkpointing schedules such that the number of flow recomputations is proven to be minimal.

The adjoint code based on these advanced AD techniques precisely performs the fixed point scheme in Eq. (7) and the sensitivity evaluation in Eq. (8). Since the exact differentiation of the fixed point iterator G is maintained, the consistency and accuracy of the adjoint solver is still preserved. The performance of the adjoint RANS solver in accurate computation of sensitivities has been successfully demonstrated on industrial high-lift configurations [19, 20].

3 Computational Setup

3.1 Configuration Details

The test case under investigation is the industry relevant swept constant-chord half-model (SCCH) high-lift configuration. This configuration consists of a main wing with extended slat and flap. All devices have blunt trailing edges. The three-dimensional wing has a sweep angle of $\phi = 30^{o}$ while the chord length in the spanwise direction is kept constant. In order to reduce the computational costs, numerical investigations are performed on an infinite span wing. Figure 1 shows a two-dimensional section of the high-lift configuration. The relative chord lengths of slat and flap are given by $l_{slat} = 0.158 l_c$ and $l_{flap} = 0.254 l_c$, where l_c is the chord length. The angle of attack is fixed at $AoA = 6^{o}$, which is within the range of approach for civil aircraft. The flap deflection angle is set to $\delta_{flap} = 37^{o}$. Note that, at these conditions, the flow over the slat and the main wing are fully attached. On the other hand, the flow over the flap is separated starting from the shoulder region as the point of separation reaches its most upstream position. Therefore, the above settings are best suited for the application of active flow control mechanism to delay the separation and thus enhance the aerodynamic performance of the SCCH high-lift configuration.

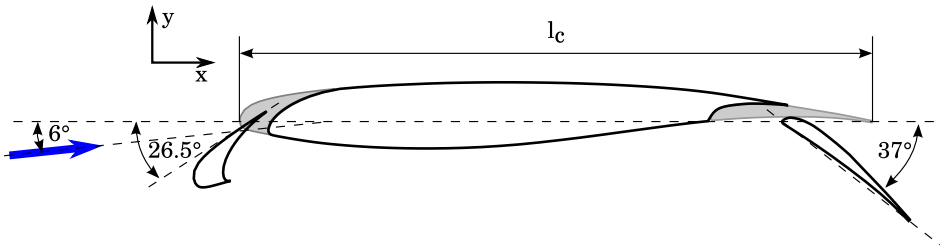

Figure 1: Sketch of a three-element high-lift configuration.

3.2 Computational Mesh

Figure 2 shows the two-dimensional mesh around the SCCH high-lift configuration. The computational domain consists of a C-type block-structured mesh with $43,098$ finite volumes. The three-dimensional mesh for the infinite span wing is generated by stacking 16 layers of the two-dimensional mesh along the spanwise direction and applying the respective sweep angle. The resulting domain consists of a block-structured mesh with $689,568$ finite volumes. Figure 3 shows the surface mesh around the slat, main wing and the flap. The non-dimensional wall distance of the first cell center remains below $y^+ = 1$ on the entire surface.

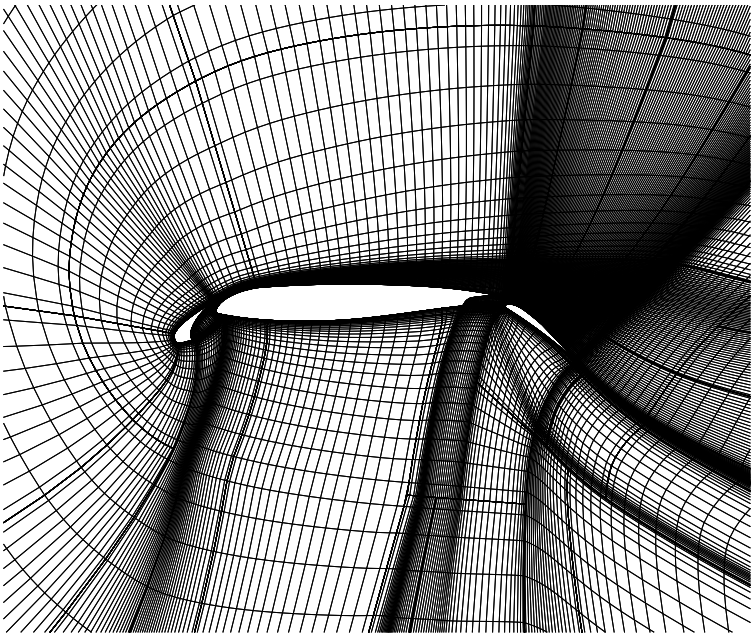

Figure 2: Two-dimensional grid around the SCCH high-lift configuration.

3.3 Boundary Conditions

At the inlet boundary, all flow quantities including the components of the velocity vector and turbulent quantities are prescribed. At the outflow boundary, a convective boundary condition is used that allows the unsteady flow structures to be transported outside the computational domain. On the surface of the main wing, flap and slat, no-slip boundary condition is applied. For the calculation of the infinite span swept wing, a periodic boundary condition is employed. To model the active flow control mechanism, synthetic jet actuation is applied on the flap surface at 27 slots along the chordwise direction at all the 16 grid layers along the spanwise direction. Figure 4 shows the distribution of actuation slots on the surface of the flap. Numerically, each slot is resolved by one cell face on the flap surface. The actuation velocity at a slot face is given by

$$\vec{u} = A u_\infty \left[\vec{n} + \frac{1}{\tan \beta_1} \vec{t_1} + \frac{1}{\tan \beta_2} \vec{t_2} \right] \cos\left(2\pi f \left(t - t_0\right)\right) \tag{9}$$

Here $\vec{n}$ is the surface normal vector while $\vec{t_1}$ and $\vec{t_2}$ are a set of tangential vectors. A is the non-dimensional amplitude of actuation, u_∞ is the free-stream velocity, β_1 and β_2 are the blowing angles, f is the non-dimensional frequency, t is the non-dimensional physical time and t_0 is the non-dimensional phase shift.

3.4 Numerical Flow Solvers

In the present work, the unsteady Reynolds-averaged Navier-Stokes equations are solved using the CFD code ELAN [6, 8]. ELAN is a multi-purpose finite volume solver based on the SIMPLE pressure-velocity

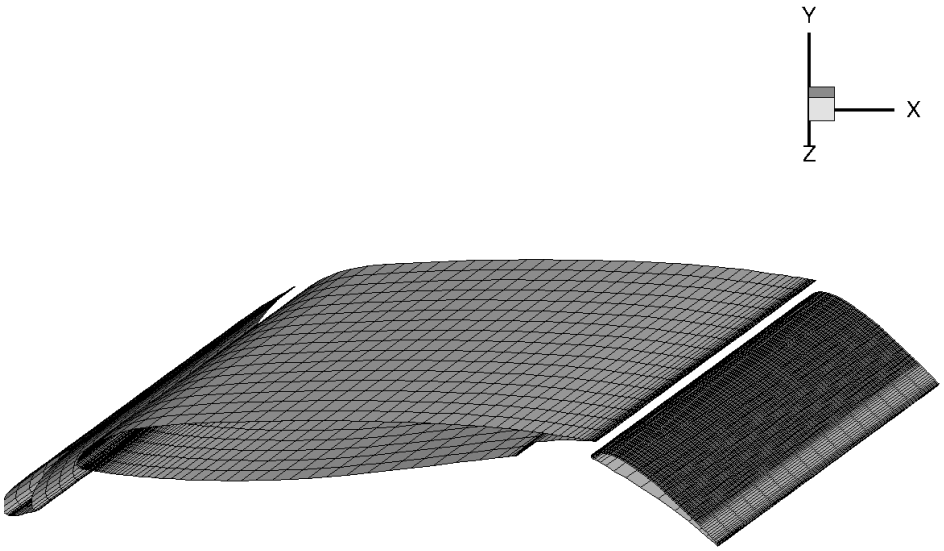

Figure 3: Surface grid around the SCCH high-lift configuration.

coupling scheme for the solution of incompressible Navier-Stokes equations. The code is fully implicit and is of second order accuracy both in space and time. The convective fluxes are approximated by a TVD-MUSCL scheme. The code can be run in unsteady RANS mode with options for various statistical turbulence models or in LES mode or a combination of both. The code is parallelised by domain decomposition and uses a message passing interface (MPI) for the communication between the nodes of a supercomputer. ELAN has been successfully used to perform unsteady RANS and DES simulations on practical high-lift configurations [6, 8]. The unsteady discrete adjoint RANS code ELAN-A [21, 20] is developed by applying the AD tool Tapenade [22] to the primal unsteady RANS code ELAN. ELAN-A retains all features of the primal code ELAN. Performance measurements have shown that the run-time of the adjoint code ELAN-A is around a factor of 5 compared to the primal code. Although it may not be as computationally efficient as the hand differentiated code, the lack of efficiency is well compensated by accuracy, robustness and easy maintenance.

4 Numerical Results

4.1 Un-actuated baseline flow

We first consider the un-actuated baseline flow around the SCCH high-lift configuration. The unsteady incompressible RANS simulations are performed with the SST $k-\omega$ turbulence model at a Reynolds number of $Re = 10^6$ and at an angle of attack of $AoA = 6^o$. The step size in the time discretisation scheme is chosen as $\Delta t = 2 \times 10^{-3} l_c/u_\infty$, which is sufficient to resolve and capture most of the unsteady flow features. Figure 5 shows the isosurfaces of λ_2 - vortex cores coloured by u - velocity at the crest of a periodic oscillation in the lift coefficient. It can be observed that the unsteady RANS simulations predict the required massive separation of the flow due to strong adverse pressure gradient on the suction side of the flap. The mean separation point is located just behind the flap leading edge. Downstream of the separation point is a large region of recirculation zone, which is most suited for the application of active flow control techniques. The mean lift coefficient for the un-actuated flow is observed to be $\overline{C}_l = 1.0198$.

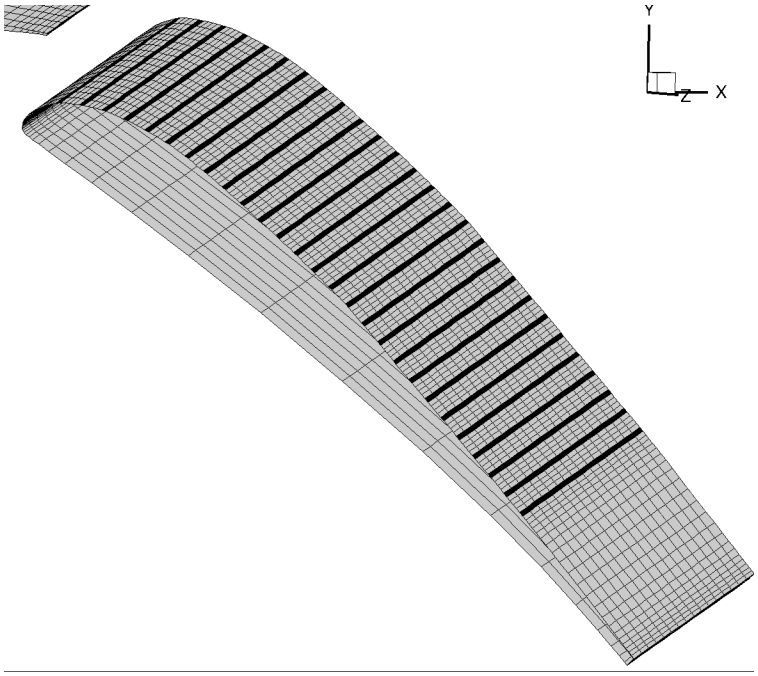

Figure 4: Distribution of actuation slots on the surface of the flap of the SCCH high-lift configuration.

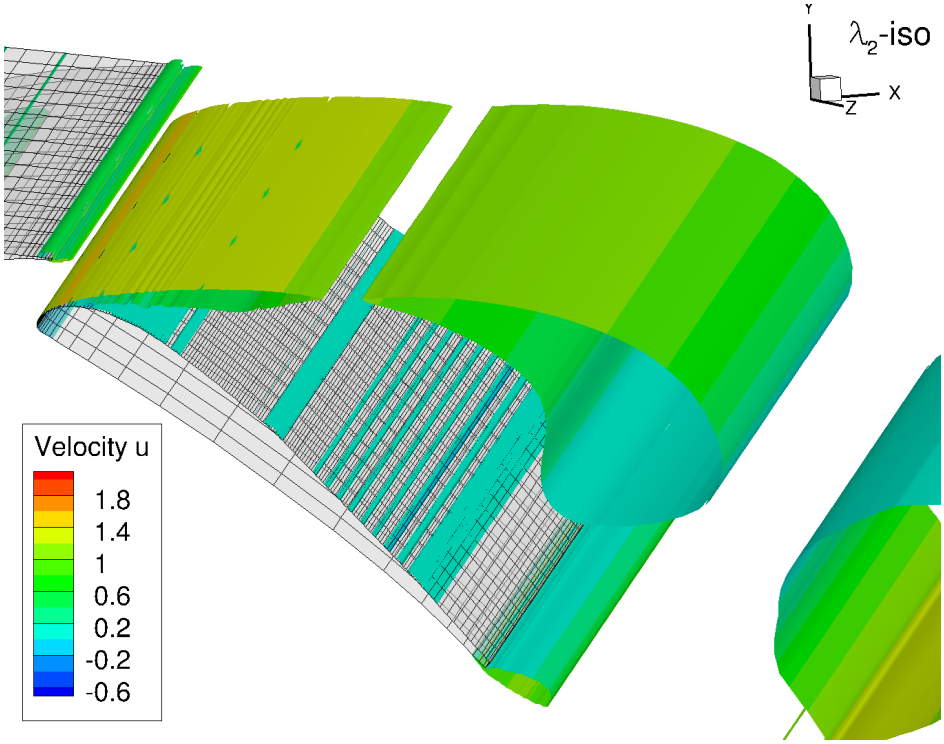

Figure 5: Un-actuated baseline flow: Isosurfaces of the λ_2 - vortex cores near the flap region.

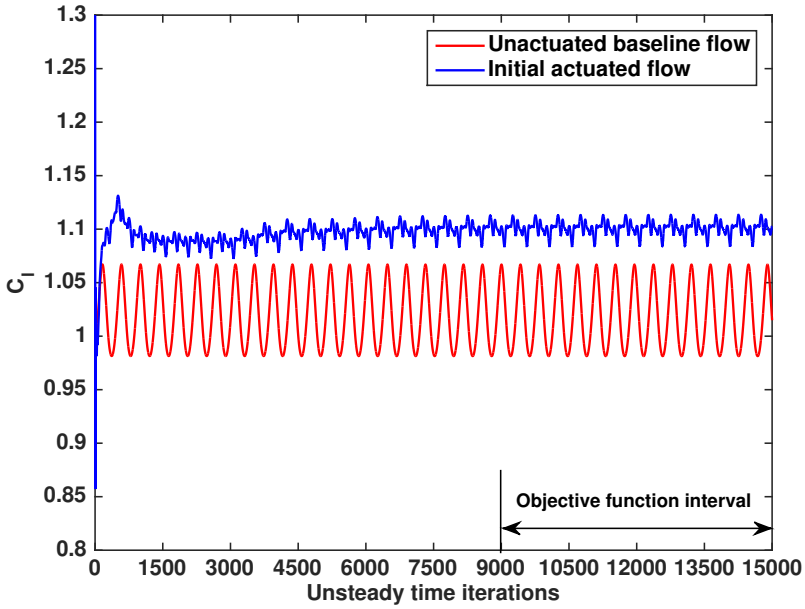

Figure 6: Time history of the lift coefficients for the un-actuated baseline flow and the initial actuated flow.

4.2 Initial actuated flow

In order to delay the flow separation and to enhance the overall aerodynamic performance of the SCCH high-lift configuration, sinusoidal blowing and suction with zero-net-mass-flux actuation is applied at 432 actuation faces on the suction side of the flap, as shown in Figure 4. To start the optimisation, initially the non-dimensional values of actuation parameters are chosen as $A = 0.3$, $f = 2.0$ Hz, $\beta_1 = 90^o$, $\beta_2 = 90^o$, and $t_0 = 0$. At blowing angles of 90^o, the flow is perturbed in the normal direction of the flap surface. The frequency of the initial actuation is set to the estimated frequency of the vortex shedding of the un-actuated baseline flow. Unsteady RANS simulations are performed with the initial control starting from a fully developed baseline flow until the non-dimensional time $T = 30$, which amounts to $15,000$ unsteady time iterations. Figure 6 shows the time history of the lift coefficient. Compared to the un-actuated flow with $\overline{C}_l = 1.0198$, the initial actuation has resulted in 8% improvement in the mean-lift coefficient with $\overline{C}_l = 1.1008$.

Although, the initial actuation has considerably improved the lift over the baseline flow, it may not be the optimal actuation and therefore the mean-lift thus achieved may not be maximum. The objective is to find optimal actuation that suppresses or even delays the separation and enhances the aerodynamic performance in terms of lift. For the optimisation problem, we neglect the initial transient behaviour in the lift coefficient of the controlled flow, as shown in Figure 6. The objective function, which is the time-averaged lift coefficient is then evaluated over a fully developed flow starting from $9,001$ to $15,000$ time iterations. Note that this interval consists of around 11 actuation cycles, which is sufficiently large for a meaningful average of the developed flow. The discrete objective function defined over this interval is then given by

$$J = \overline{C}_l = \frac{1}{6,000} \sum_{n=9,001}^{15,000} C_l^n \left(\boldsymbol{U}^n, \boldsymbol{\alpha} \right) \tag{10}$$

while the associate Lagrangian reduces to

$$L = \frac{1}{6,000} \sum_{n=9,001}^{15,000} C_l^n - \sum_{n=1}^{15,000} \left[\left(\overline{\boldsymbol{U}}^n \right)^T \left(\boldsymbol{U}^n - \boldsymbol{G}^n \right) \right] \tag{11}$$

The control variables are the actuation amplitudes, blowing angles and phase shifts at 432 actuation faces on the flap surface. Note that the frequency of the actuation is kept constant at all actuation faces throughout the optimisation process. This results in a total of $1,728$ control variables.

4.3 Sensitivity validation

We now demonstrate the performance of the unsteady discrete adjoint incompressible RANS solver in accurate computation of actuation sensitivities. Table 1 shows a comparison of the sensitivities at a randomly chosen actuation face. It can be observed that the sensitivities based on the adjoint code are in very good agreement with the values obtained from the AD based tangent linear code and second order finite differences. Note that the discrepancy in sensitivities is due to the accumulation of computational noise in fixed point iterations over a large time interval, as defined in Eqs. (10) and (11). In the present case, the computational noise arises predominantly due to truncation error.

Control parameter	Finite differences	Tangent linear code	Adjoint code
Amplitude A	-2.53482457E-03	-2.53487987E-03	-2.53483821E-03
Phase shift t_0	-4.56140902E-03	-4.56140383E-03	-4.56125074E-03
Blowing angle β_1	1.44098066E-06	1.44093624E-06	1.44093936E-06
Blowing angle β_2	3.08708614E-07	3.08897284E-07	3.08907451E-06

Table 1: Comparison of the actuation parameter sensitivities at a randomly selected actuation face based on second order finite differences, tangent linear and discrete adjoint unsteady RANS codes.

4.4 Optimal actuation

To find the optimal actuation, the unsteady adjoint RANS solver is combined with the quasi-Newton BFGS optimisation algorithm. Figure 7 shows the time history of the lift coefficient for the optimal actuated case. It is clearly evident that the optimal actuation has yielded significant enhancement in the lift coefficient over the un-actuated and initial actuated flows. Table 2 shows a comparison of the mean-lift coefficient. From the tabulated values, it can be observed that the optimal actuation improved the mean-lift by 28% compared to the un-actuated baseline flow and around 19% over the initial actuation. Figure 8 shows the progress of the mean-lift coefficient during 40 cycles of optimisation. The optimisation history clearly shows that there is scope for further enhancement in the lift coefficient. Figure 9 shows the isosurfaces of λ_2 - vortex cores at the crest of a periodic oscillation in the lift coefficient. It can be noticed that the separation point has moved further downstream of the flap shoulder region.

Flow	Mean-lift coefficient
Un-actuated baseline flow	1.0198
Initial actuated flow	1.1008
Optimal actuated flow	1.3072

Table 2: Comparison of the mean-lift coefficient for the un-actuated, initial and optimal actuated flows.

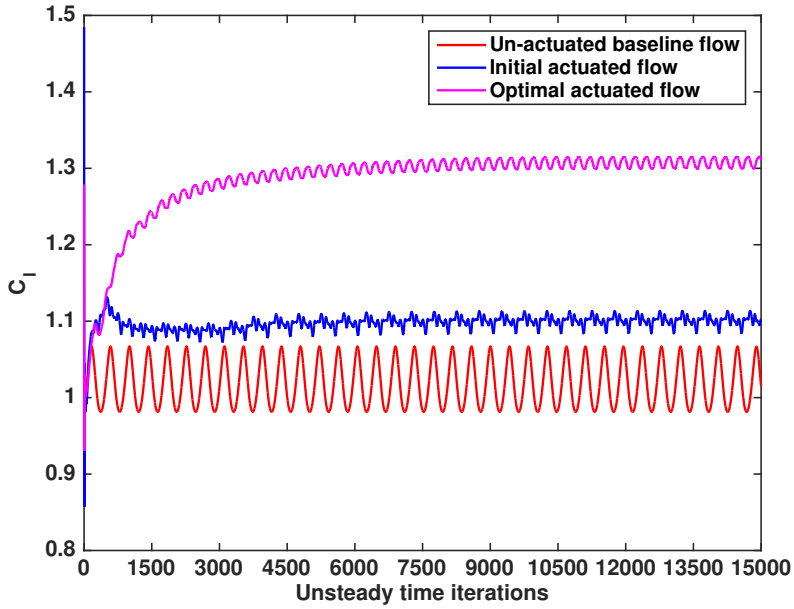

Figure 7: Time history of the lift coefficients for the un-actuated, initial and optimal actuated flows.

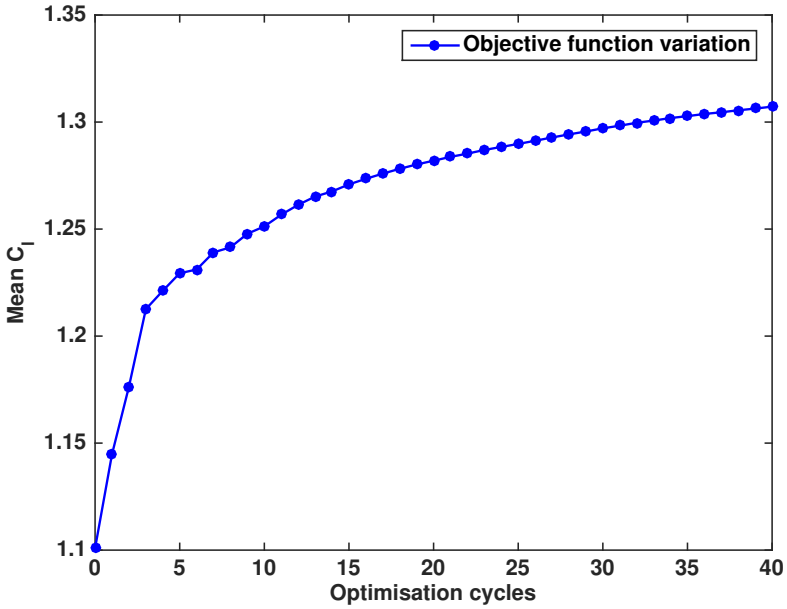

Figure 8: Variation of the mean-lift coefficient with the number of optimisation cycles.

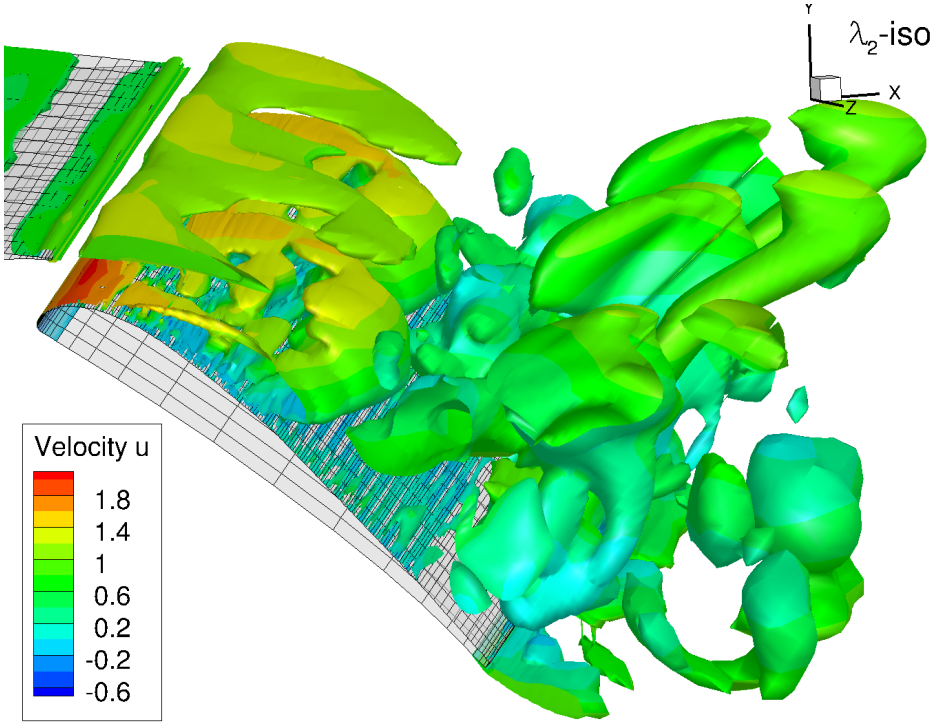

Figure 9: Optimal actuated flow: Isosurfaces of the λ_2 - vortex cores near the flap region.

Figures 10 to 13 show a comparison of the initial and optimal actuation controls and sensitivities. Figure 10(b) shows the amplitude sensitivities for the initial control with amplitude $A = 0.3$ at all actuation faces. Note that a positive sensitivity at an actuation face favours an increase in amplitude. On the other hand, negative sensitivities indicate that the initial amplitude is more than sufficient and needs to be decreased. From the sensitivity plot one can observe a strong positive sensitivity across the span wise direction just downstream of the shoulder region. It is clear that this region is favourable for more amplitude, as noticed in optimal amplitude control. From the optimal sensitivities one can observe that the optimisation process favours further reduction in amplitude values at actuation faces near the shoulder region. Furthermore, the sensitivities are varying along the span wise direction. This phenomena can be attributed to the effect of cross flows. One can also observe high sensitivity hot spots at actuation faces close to the trailing edge. These hot spots stresses the need for further optimisation and they may dampen subsequently.

One can draw similar arguments from the phase shift control and sensitivity plots in Figure 11. Figures 12 and 13 show the corresponding plots for the actuation blowing angles β_1 and β_2. From these plots it can be observed that the angle sensitivities are negligible to influence changes in control vectors. In fact, the angle sensitivities may support the argument that the actuation normal to the flap surface is favourable for optimal control.

To summarise, the numerical results clearly demonstrate that the adjoint approach is promising in finding the optimal actuation mechanism on the high-lift configuration. It is possible to enhance the aerodynamic performance further by combining the adjoint based gradient search method with evolutionary algorithms. In [23], this hybrid approach is successfully applied to completely suppress the flow separation on the flap of a three-element airfoil. In fact, optimisation has significantly increased the mean-lift by 67% over the un-actuated baseflow. In future, we plan to extend this approach to the SCCH high-lift configuration.

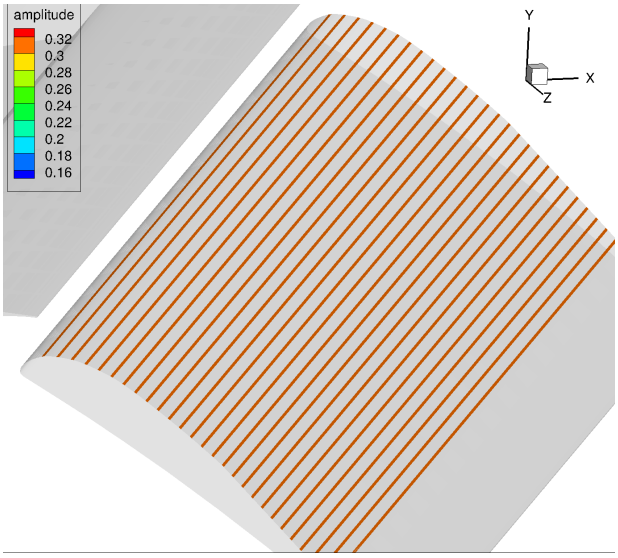

(a) Initial amplitude control

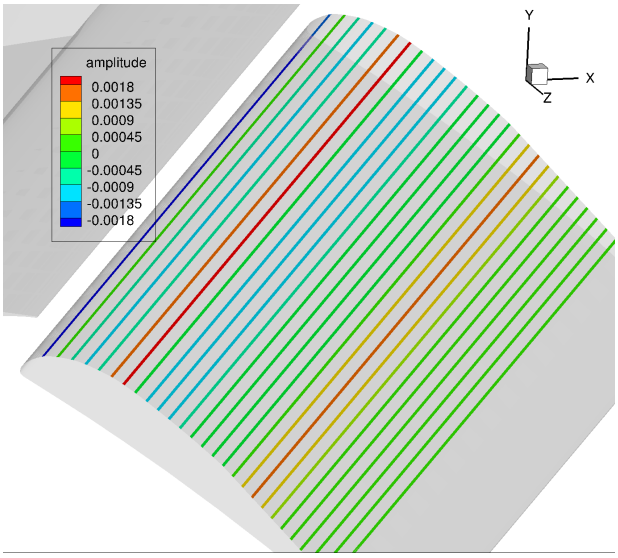

(b) Initial amplitude sensitivity

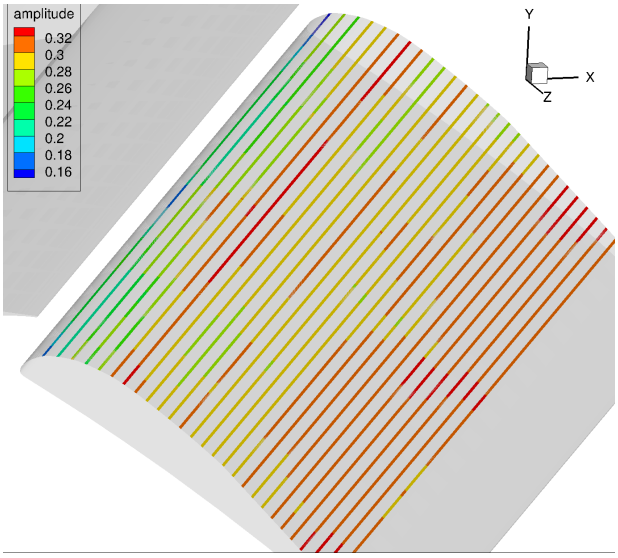

(c) Optimal amplitude control

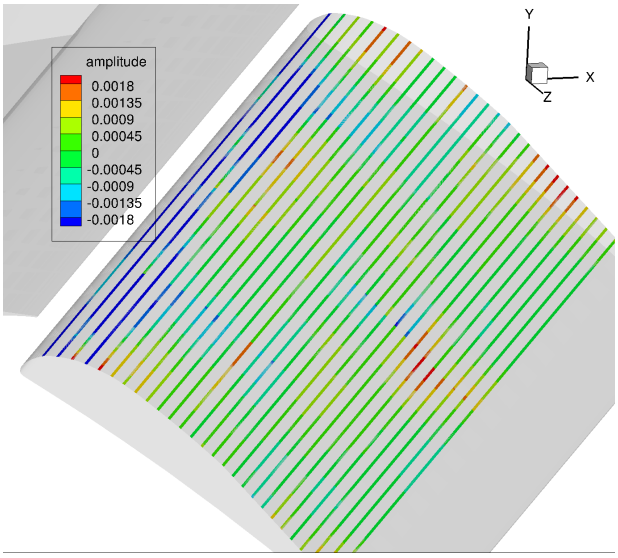

(d) Optimal amplitude sensitivity

Figure 10: Comparison of the initial and optimal amplitude controls and sensitivities.

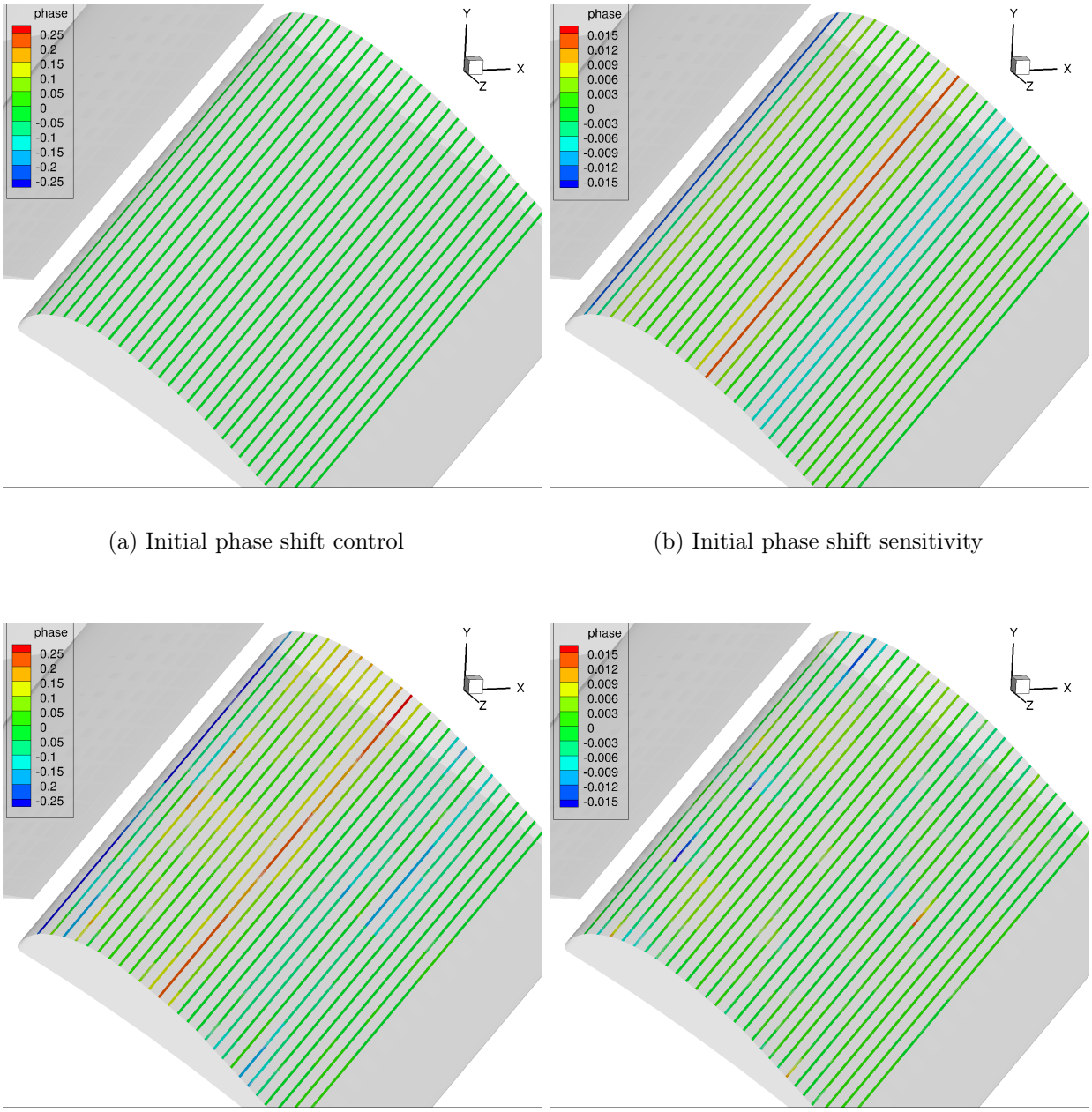

(a) Initial phase shift control

(b) Initial phase shift sensitivity

(c) Optimal phase shift control

(d) Optimal phase shift sensitivity

Figure 11: Comparison of the initial and optimal phase shift controls and sensitivities.

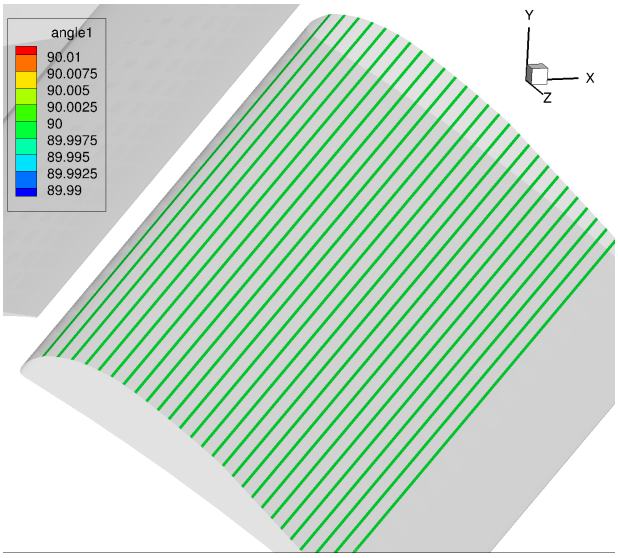

(a) Initial angle β_1 control

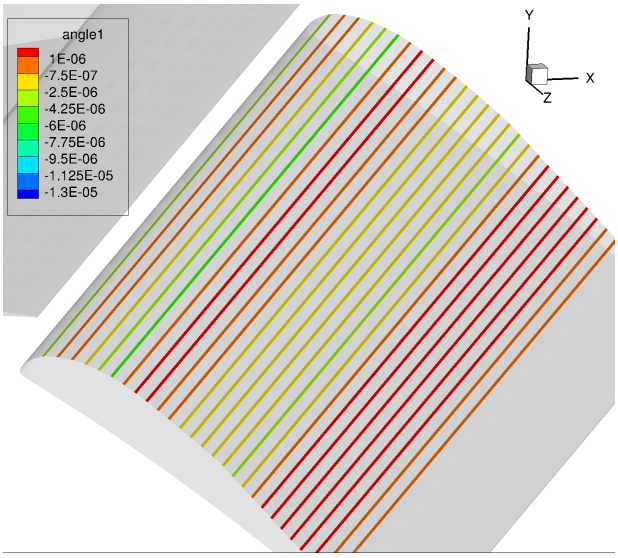

(b) Initial angle β_1 sensitivity

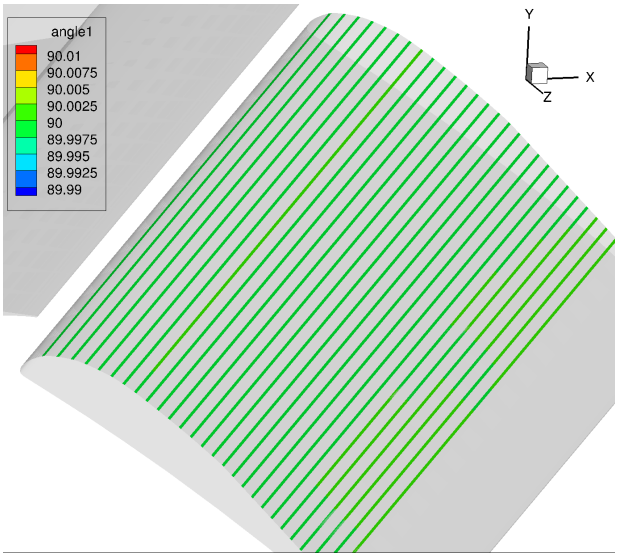

(c) Optimal angle β_1 control

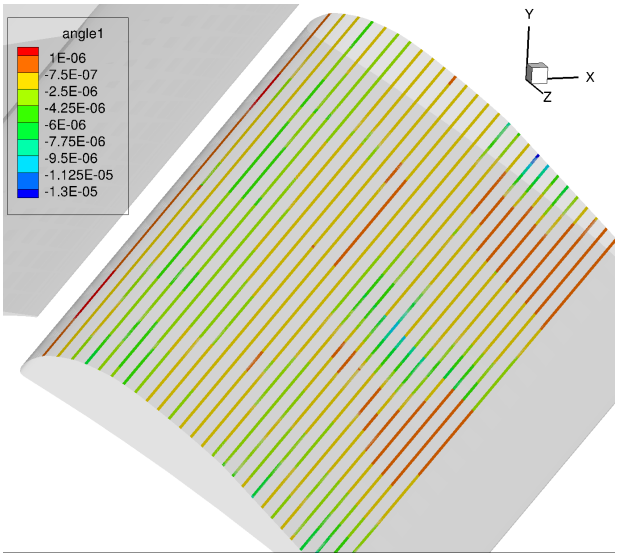

(d) Optimal angle β_1 sensitivity

Figure 12: Comparison of the initial and optimal angle β_1 controls and sensitivities.

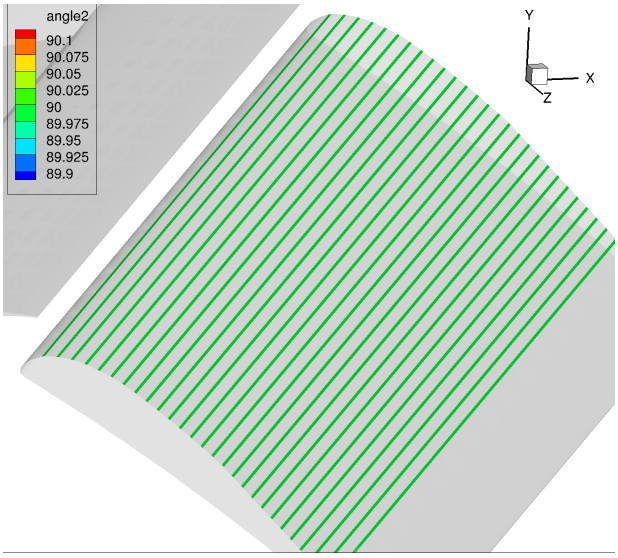

(a) Initial angle β_2 control

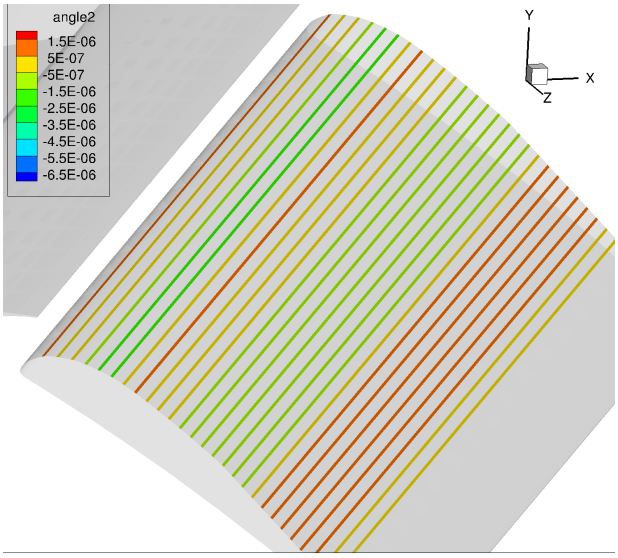

(b) Initial angle β_2 sensitivity

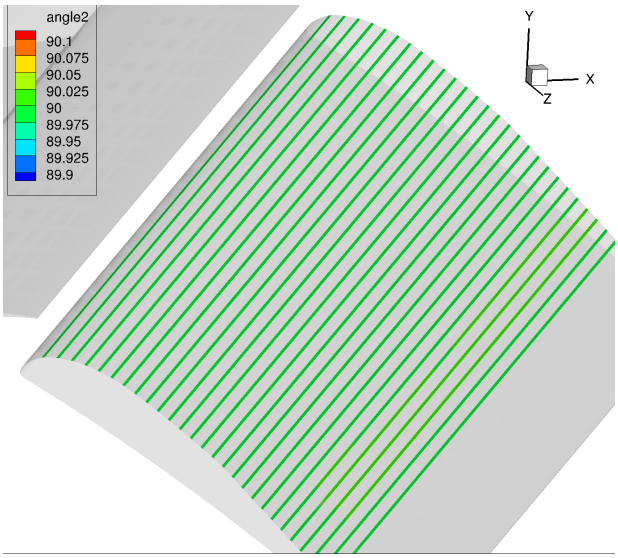

(c) Optimal angle β_2 control

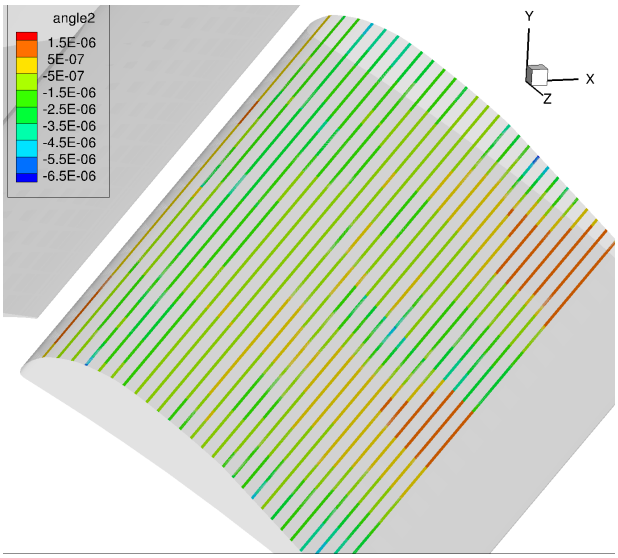

(d) Optimal angle β_2 sensitivity

Figure 13: Comparison of the initial and optimal angle β_2 controls and sensitivities.

5 Conclusions

In this paper, we presented an optimal active separation control on the Swept Constant Chord Half model (SCCH) high-lift configuration at a Reynolds number of $Re = 10^6$ and an angle of attack of 6^o. To delay the flow separation, the zero-net-mass-flux synthetic jet actuation was applied on the suction side of the flap. The optimal set of actuation parameters that delays the separation was obtained by combining the unsteady incompressible discrete adjoint RANS solver with the BFGS optimisation algorithm. The performance of the adjoint RANS solver in accurate computation of actuation sensitivities was successfully demonstrated by comparing the adjoint sensitivities with the values obtained from finite differences and tangent linear RANS solver. Numerical results have shown that the optimal actuation has delayed the separation further downstream and significantly enhanced the mean-lift by 28% over the un-actuated baseline flow.

Acknowledgements

The authors gratefully acknowledge the computing time granted by the Allianz für Hochleistungsrechnen Rheinland-Pfalz (AHRP), Germany.

References

[1] M. Gad-el Hak and M. D. Bushnell. Separation control: Review. *Journal of Fluids Engineering*, 113(5):5–30, 1991.

[2] M. Gad-el Hak. Flow control: The future. *Journal of Aircraft*, 38(3):402–418, 2001.

[3] S. S. Collis, R. D. Joslin, A. Seifert, and V. Theofilis. Issues in active flow control: theory, control, simulation, and experiment. *Progress in Aerospace Sciences*, 40(4):237–289, 2004.

[4] L.P. Melton, C.S. Yao, and A. Seifert. Application of excitation from multiple locations on a simplified high-lift system. AIAA Paper 2004-2324, 2004.

[5] A. Khodadoust and A. Washburn. High Reynolds number simulations of distributed active flow control for a high-lift system. AIAA Paper 2007-4423, 2007.

[6] B. Günther, F. Thiele, W. Petz, R. Nitsche, J. Sahner, T. Weinkauf, and H. C. Hege. Control of seperation on the flap of a three-element high-lift configuration. AIAA Paper 2007-0265, 2007.

[7] M. Bauer, I. Peltzer, W. Nitsche, and B. Gölling. Active flow control on an industry-relevant civil aircraft half model. *Notes on Numerical Fluid Mechanics and Multidisciplinary Design*, 108:95–107, 2010.

[8] T. Höll, A. K. V. Job, P. Giacopinelli, and F. Thiele. Numerical study of active flow control on a high-lift configuration. *Journal of Aircraft*, 49(5):1406–1422, 2012.

[9] V. Ciobaca, T. Kühn, R. Rudnik, M. Bauer, B. Gölling, and W. Breitenstein. Active flow separation control on a high-lift wing-body configuration. *Journal of Aircraft*, 50(1):56–72, 2013.

[10] B. L. Smith and A. Glezer. The formation and evolution of synthetic jets. *Physics of Fluids*, 10(9):2281–2297, 1998.

[11] A. Glezer and M. Amitay. Synthetic jets. *Annual Review of Fluid Mechanics*, 34:503–529, 2002.

[12] A. Nemili, E. Özkaya, N. Gauger, F. Kramer, and F. Thiele. Optimal separation control on the flap of a 2D high-lift configuration. *Computational Methods in Applied Sciences*, 36:411–425, 2015.

[13] R. Petz and W. Nitsche. Active control of flow separation on a swept constant chord half model in a high-lift configuration. AIAA Paper 2006-3505, 2006.

[14] T. Höll, E. Wassen, and F. Thiele. Numerical investigation of spatially distributed actuation on a three-element high-lift configuration. *Notes on Numerical Fluid Mechanics and Multidisciplinary Design*, 108:109–123, 2010.

[15] T. Höll, E. Wassen, and F. Thiele. Active separation control on a high-lift configuration using segmented actuation slots. AIAA Paper 2010-4249, 2010.

[16] A. Griewank and A. Walther. *Evaluating derivatives: Principles and techniques of Algorithmic Differentiation*. SIAM, 2008.

[17] B. Christianson. Reverse accumulation of attractive fixed points. *Optimization Methods and Software*, 3:311–326, 1994.

[18] A. Griewank and A. Walther. Revolve: An implementation of checkpointing for the reverse or adjoint mode of computational differentiation. *ACM Transactions on Mathematical Software*, 26:19–45, 2000.

[19] A. Nemili, E. Özkaya, N. Gauger, F. Kramer, T. Höll, and F. Thiele. Optimal design of active flow control for a complex high-lift configuration. *AIAA Paper 2014–2515*, 2014.

[20] A. Nemili, E. Özkaya, N. Gauger, F. Kramer, and F. Thiele. Discrete adjoint based optimal active control of separation on a realistic high-lift configuration. *Notes on Numerical Fluid Mechanics and Multidisciplinary Design*, 132:237–246, 2016.

[21] A. Nemili, E. Özkaya, N. Gauger, F. Kramer, A. Carnarius, and F. Thiele. Discrete adjoint based sensitivity analysis for optimal flow control of a 3D high-lift configuration. *AIAA Paper 2013–2585*, 2013.

[22] L. Hascoët and V. Pascual. The Tapenade Automatic Differentiation tool: Principles, Model, and Specification. *ACM Transactions On Mathematical Software*, 39(3), 2013.

[23] A. Nemili, E. Özkaya, N. Gauger, F. Kramer, and F. Thiele. A two-level hybrid approach for optimal active flow control on a three-element airfoil. *Proceedings of the ECCOMAS Conference*, 2016.